

U and Th zonation in apatite observed by laser ablation ICPMS, and implications for the (U–Th)/He system

K.A. Farley^{a,*}, D.L. Shuster^{b,c}, R.A. Ketcham^d

^a *Division of Geological and Planetary Sciences, Caltech, MS 170-25, Pasadena, CA 91125, USA*

^b *Berkeley Geochronology Center, University of California-Berkeley, Berkeley, CA 94720, USA*

^c *Dept. of Earth and Planetary Science, University of California-Berkeley, Berkeley, CA 94720, USA*

^d *Department of Geological Sciences, University of Texas-Austin, Austin, TX 78712, USA*

Received 26 January 2011; accepted in revised form 13 May 2011; available online 25 May 2011

Abstract

A laser-ablation inductively-coupled plasma mass spectrometry technique was developed to measure U, Th, and Ce zonation in polished sections of apatite for assessing the consequences of parent zonation for (U–Th)/He thermochronometry. The technique produces concentration maps with an averaging length-scale of ~ 20 μm , comparable to the α -stopping distance, and a precision of $\sim 5\%$ down to few ppm concentration levels. A model was developed to transform the measured concentration distribution into a simplified representation for use in spherical-geometry He production–diffusion models. To illustrate these methods, 30 sections of apatite from a single granite (GC863) were mapped. Every analyzed apatite from GC863 is zoned, with most grains having variable thickness rims and terminations that are enriched in U and Th by about a factor of three over the grain cores.

Parent zonation has three independent effects on (U–Th)/He He ages: it influences the α ejection correction, the ^4He concentration profile which governs diffusive loss, and, via radiation damage trap accumulation, spatial variability of diffusivity within the crystal. If the observed zonation is typical of the apatite population in GC863, use of the standard homogenous α ejection correction would cause He ages to be on average 3% too young, and with a large amount of grain-to-grain variability (9% too young in the most rim-enriched case to 6% too old in a core-enriched case). Independent of the ejection correction, the concentration profile modifies the effective closure temperature of the apatites by placing more (or less) ^4He near the grain edge. The parent zonation in GC863 apatites causes closure temperatures to range from four degrees lower (rim-enriched case) to two degrees higher (core-enriched case) than applies in the homogenous case. Alpha ejection and concentration profile effects on He age are additive and of the same sense. In the case of typical grains in GC863 cooled between 1 and 10 $^{\circ}\text{C}/\text{Ma}$, the two effects are roughly equal in magnitude. The effects of intracrystalline variations in radiation damage trap accumulation become apparent at slow cooling rates (1 $^{\circ}\text{C}/\text{Ma}$). For example, in rim-enriched GC863 grains cooled at 1 $^{\circ}\text{C}/\text{Ma}$, preferential accumulation of radiation damage traps near the grain rim almost compensates for the higher loss rate expected of ^4He also located preferentially near the rim. Under some circumstances strong rim-enrichment may actually increase the effective closure temperature of an apatite. Zonation at the level observed in GC863 modifies the $^4\text{He}/^3\text{He}$ spectra substantially from that expected from a uniform distribution. Measured $^4\text{He}/^3\text{He}$ spectra are strikingly similar to predictions based on the mapped eU distributions of the very same crystals, supporting the overall validity of the analytical and interpretive approach presented here.

The magnitude and style of U, Th zonation documented in GC863 is one possible source of frequently observed overdispersion of apatite (U–Th)/He ages as well as anomalous $^4\text{He}/^3\text{He}$ spectra.

© 2011 Elsevier Ltd. All rights reserved.

* Corresponding author.

E-mail addresses: farley@gps.caltech.edu (K.A. Farley), dshuster@bgc.org (D.L. Shuster), ketcham@mail.utexas.edu (R.A. Ketcham).

1. INTRODUCTION

(U–Th)/He dating is based on the ingrowth of ^4He from the α decay of U and Th (Strutt 1908; Hurley, 1954; Farley, 2002). While the technique has occasionally been used to determine the age of volcanic rocks (Farley et al., 2002; Davidson et al., 2004) its dominant application has been to thermochronometry, especially of apatite (Zeitler et al., 1987; Lippolt et al., 1994; Ehlers and Farley, 2003). Most commonly, cooling histories are established by measuring the (U–Th)/He age of a crystal and comparing it with ages modeled (Wolf et al., 1998; Ketchum, 2005) using the He production–diffusion equation calibrated by laboratory-based He diffusion kinetic parameters. Apatite (U–Th)/He thermochronometry is particularly useful because the system has a closure temperature lower than other techniques, about 55–80 °C depending on the amount of radiation damage in the grain (Flowers et al., 2009; Gautheron et al., 2009). Complementary information on an apatite's cooling path can be obtained from the ^4He concentration profile revealed by the $^4\text{He}/^3\text{He}$ method (Shuster and Farley, 2004).

While in many cases apatite He ages and $^4\text{He}/^3\text{He}$ spectra are reproducible, consistent with other thermochronometric techniques, and geologically reasonable, it is clear that problematic results are occasionally obtained. In some cases replicate apatite He ages scatter far more than can be attributed to analytical uncertainty (e.g., Belton et al., 2004). In other cases apatite He ages are older than expected based on geologic constraints, or, more commonly, from a comparison with apatite fission track ages (e.g., Green et al., 2006). Similarly, some apatite $^4\text{He}/^3\text{He}$ spectra are inconsistent with expectations of He production and diffusion in a system with a uniform distribution of U and Th (Farley et al., 2010). Here we present techniques for measuring and evaluating one possible cause of these problematic results: inhomogeneous distribution of U and Th in the apatites. This work builds on a related study by Hourigan et al. (2005) concerned primarily with zonation in zircon.

Alpha particles produced by U and Th are emitted with significant kinetic energy and come to rest after traversing $\sim 20\ \mu\text{m}$ of solid matter. As a result, daughter ^4He atoms are not located precisely at the site of their parent. Because $20\ \mu\text{m}$ is fairly large compared to the typical dimensions of an apatite crystal, some α particles will be ejected from the crystal. Geometric models have been presented that permit correction for this effect if the parent distribution is homogeneous (Farley et al., 1996). More detailed models permit correction for heterogeneous distributions (Hourigan et al., 2005), but are almost never applied because the parent nuclide distributions are not commonly measured. Thus errors in the α ejection correction factor (F_T) arising from inaccuracy of the commonly-assumed uniform parent distributions may be a source of unquantified error in apatite He ages. In addition to affecting F_T , inhomogeneous distribution of parent nuclides modifies the ^4He concentration gradient. This modification can affect the ^4He ages since it is this gradient that governs diffusive loss. Similarly the $^4\text{He}/^3\text{He}$ technique, which documents the ^4He concentra-

tion gradient, is sensitive to the parent nuclide distribution (Shuster and Farley, 2004; Farley et al., 2010). Finally, because He diffusion rates are sensitive to radiation damage density in apatite (Shuster and Farley, 2009), intracrystalline variations in U and Th distribution can cause intracrystalline variations in He diffusivity.

Only limited quantitative information exists on the spatial distribution of U and Th in apatite. The ppm concentrations of these elements are usually too low to be measured by electron microprobe. Fission tracks reveal the U distribution in apatites subjected to fission track dating, but we are unaware of published U maps of the requisite detail for our work, and in any case fission tracks cannot be used to map Th. Jolivet et al. (2003) used laser ablation inductively coupled plasma mass spectrometry (LA-ICPMS) on a zoned apatite sample and found strong correlations among the concentrations of Ce, U, and Th as well as cathodoluminescence (CL) intensity. Based on these results they highlighted the importance of zonation in apatite thermochronometry and suggested that CL intensity and Ce concentration measured by electron microprobe might offer inexpensive proxies of U, Th zonation. Boyce and Hodges (2005) made similar observations on a Durango apatite megacryst. Here we further develop the use of LA-ICPMS for observing apatite U and Th distributions. The technique we present is applicable to measuring trace element distributions in general, but the various parameter tradeoffs that exist in the LA-ICPMS measurement and data reduction scheme have been chosen specifically to address issues arising in (U–Th)/He dating. Our approach and goals are similar to the earlier work on zircon (Hourigan et al., 2005), but we measured parent nuclide distributions on a polished section, rather than in a drilling mode. It is also similar to the study of Durango apatite (Boyce and Hodges, 2005), but considers apatites of more typical size and origin.

In the first part of this paper we describe the analytical method as well as techniques for converting the measured results into a concentration map. In the second part we address the question of how a concentration map can be converted into a distribution that is useful for apatite He production–diffusion models. Finally, we present maps of U, Th, and Ce distribution from multiple apatites from a single rock to illustrate the methodology and to assess the implications of the observed zonation for both He ages and $^4\text{He}/^3\text{He}$ profiles. We compare measured $^4\text{He}/^3\text{He}$ profiles with those predicted from the zonation patterns.

2. SAMPLES AND ANALYTICAL METHODS

Apatite crystals used to illustrate the LA-ICPMS measurements and their interpretation are from a granodiorite (GC863) from the vicinity of Reference Creek Rapids in the Lower Granite Gorge of the Grand Canyon. The rock was collected by Ian Campbell on the Carnegie-Caltech 1939 Colorado River expedition and the precise sampling location was not recorded. From descriptions in Campbell's field notes we infer it is from 35°53'12.06"N, 113°42'51.38"W. Abundant large apatite crystals were obtained by standard crushing and heavy liquid separation

techniques at Caltech. Single grain α -ejection corrected ages of 72, 69, 68, 68, and 72 and a single outlier at 90 Ma will be presented and discussed elsewhere. The standard deviation of all six grain ages is $\sim 12\%$; without the 90 Ma outlier it is 3%.

Laser ablation measurements were undertaken using a Thermo X-Series 2 quadrupole ICPMS fitted with a collision cell. The ICPMS was interfaced with a New Wave UP-193 laser operating at 193 nm. Trace element concentration maps were obtained on large unbroken apatite crystals mounted in epoxy and polished following procedures typical for SEM or electron microprobe work. Concentrations were mapped on a grid of linear traverses running either perpendicular or parallel to the long axis of the crystal. Crystals of typical dimension were mapped by between 8 and 12 traverses (Figs. 1 and 2). Each traverse began and ended in epoxy so as to ensure analysis of the entire grain. The starting and ending locations of each traverse were recorded to a precision of 1 μm by the UP-193. The traverses were executed at a rate of 1 $\mu\text{m}/\text{s}$ with the laser operating at 10 Hz. The spot diameter was 20 μm and typical power delivery was 0.3 Gw/cm^2 .

Ablated material was analyzed for ^{44}Ca , ^{140}Ce , ^{232}Th , and ^{238}U in continuous 150 ms sweeps. Prior to each traverse a gas blank was measured; while the trace elements typically yielded <1 cps of blank, ^{44}Ca was often as high as several hundred cps. These background signals were unimportant because count rates for Ce, U, and Th were usually in the range of 100–10000's of cps, while the ^{44}Ca signal was typically ~ 150 kcps. Note that use of the collision cell with H_2 gas is essential to obtain low background counts on any of the Ca isotopes.

After collection the traverse data were processed in the following way. First, gas blanks were subtracted from the four measured isotopes. Next the traverse ^{44}Ca data were

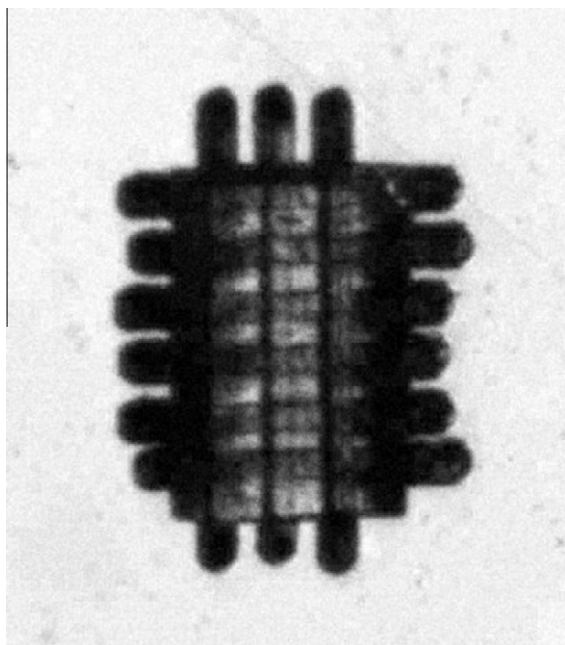


Fig. 1. Photomicrograph of an apatite grain after laser-ablation analysis. Grain is $\sim 180 \times 120 \mu\text{m}$.

scanned to identify when the beam completely intersected the apatite, as indicated by an extremely rapid rise and stabilization in beam intensity. A corresponding rapid drop in intensity was used to identify the opposite edge of the apatite. Measurements outside of the grain identified in this fashion were rejected from further processing. For each sweep the ratios $^{140}\text{Ce}/^{44}\text{Ca}$, $^{232}\text{Th}/^{44}\text{Ca}$, and $^{238}\text{U}/^{44}\text{Ca}$ were computed from blank-corrected signals assuming linear detector response for each element across the full range of signal intensity. Given a mass spectrometer sweep rate of 150 ms and a traverse velocity of 1 $\mu\text{m}/\text{s}$, each sweep is offset from the previous one by a distance of 0.15 μm . Sweeps were averaged in groups of seven to define a concentration for a specific point on the traverse; the highest and the lowest values in each group of seven were rejected to reduce high frequency fluctuations. The averaged points thus represent a sampling duration of about 1 s, equivalent to about 1 μm of separation on the traverse. Given the 20 μm spot diameter there is a large degree of overlap in the interrogated region for each successive averaged point.

For standardization, a $\sim 100 \mu\text{m}$ traverse of a fresh portion of a slab of Durango apatite was analyzed between every few unknowns over the course of the analytical session. The gas-blank-corrected $^{140}\text{Ce}/^{44}\text{Ca}$, $^{232}\text{Th}/^{44}\text{Ca}$, and $^{238}\text{U}/^{44}\text{Ca}$ ratios were averaged on the entire length of the traverse. Within each traverse the standard error of each of the mean ratios was about 2%. There was no noticeable structure within the traverses that would indicate either systematic “edge effects” as the laser impinged on the crystal, or significant concentration gradients in the crystal (Supplementary Fig. S1). The traverse mean ratios were converted into sensitivities by dividing them by the Ce, Th, and U concentrations determined on a single split of the same Durango crystal using isotope dilution solution ICPMS: 3920 ppm Ce, 190 ppm Th, 9 ppm U. Within a given laser ablation analytical session the sensitivities computed from the multiple Durango traverses had a typical 1σ variation of 4%. While there is undoubtedly some variation in the Ce, Th, and U concentrations within Durango apatite (Boyce and Hodges, 2005), the main objective of this work is to get relative concentrations rather than absolute values, so this effect is not of great consequence. We note however that for studies which require highly accurate absolute concentrations a more homogeneous concentration standard will be required. From the U and Th concentrations we computed eU (effective uranium concentration, a parameter that weights the decay of the two isotopes for their current α particle productivity, computed as $[\text{U}] + 0.235[\text{Th}]$).

The result of these calculations is a series of tightly spaced concentration determinations arrayed along 8–12 orthogonal traverses (e.g., Fig. 2). The exact location for each point was reconstructed from the starting and ending coordinates of the traverse, the traverse velocity, and the time the point measurement was obtained. The resulting irregular concentration grid was regularized using an inverse-distance-weighted algorithm (Shepard, 1968) in MATLAB with a radial distance limit of 20 μm and a power parameter of 0.7, and then plotted as a color-ramp contour plot (e.g., Fig. 3). Traverses of the Durango standard also provide an estimate of the precision of the

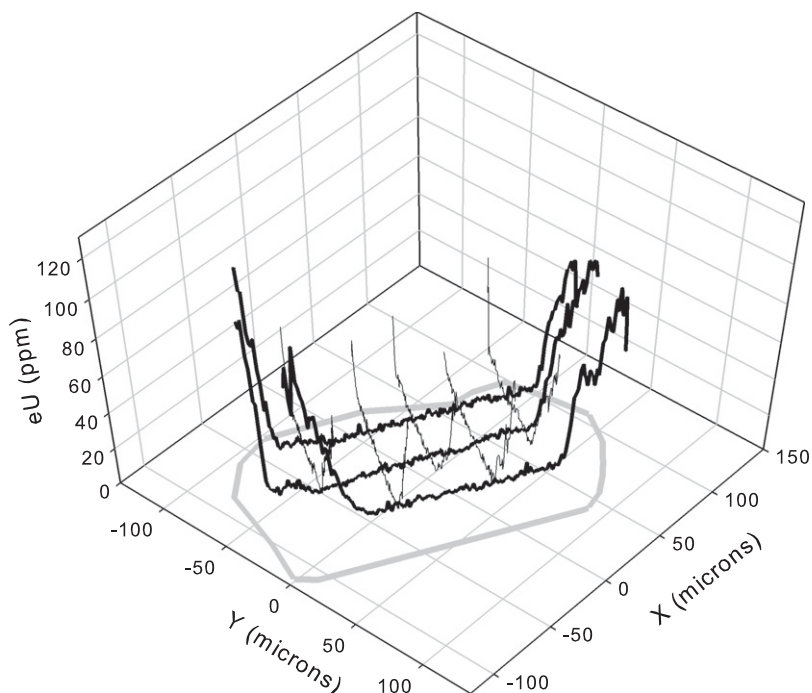


Fig. 2. Example of laser traverse data. For this sample (GC863-RD2-O) eight traverses were measured. Plotted is eU on each of the traverses (black lines) along with the outline of the crystal (light gray lines in x - y plane). These data show clearly that this crystal has low and fairly uniform concentrations in the grain interior but much higher concentrations towards the rim. See [Supplementary Fig. S7](#) for map presentation of this data.

measurements obtained in this fashion. Typically at least 40 spot measurements are averaged to obtain each point on the map. When averaged in groups of 40 spots, the standard deviation of the U, Th, and Ce concentrations along the Durango traverses is better than 5%. This variability provides a reasonable estimate of the precision of the U, Th, and Ce measurements on unknowns.

The technique we are using has multiple stages in which spatial averaging occurs; the [supplementary material](#) presents results of numerical modeling to assess the consequences of this averaging in terms of the spatial resolution obtained. These resolution tests show that the main parameter controlling the averaging length-scale is the 20 μm radius of the neighborhood used to create the uniformly-spaced concentration grid. This value is appropriate for our work because it is comparable to the distance between traverses and to the 20 μm stopping distance of α particles. Importantly, because we have already averaged over this lengthscale, in a sense the maps we produce already incorporate the alpha-redistribution phenomenon, i.e., we can consider the mapped eU distribution a reasonable approximation of the α particle production distribution (excluding the effects of ejection from the crystal).

3. CONVERTING A MAP VIEW OF CONCENTRATION INTO AN EQUIVALENT SPHERE FOR SIMULATION OF HE DIFFUSION FROM A ZONED CRYSTAL

Thus far we have been concerned with the general problem of generating a map of trace element concentration

distributions using LA-ICPMS. In this section and those that follow, we turn our attention to the particular reason we are interested in U and Th distributions in apatite: their consequences for He thermochronometry. To simplify matters, we use eU rather than the individual parent concentrations.

To convert an eU concentration map into an eU distribution that can be used in helium production–diffusion models ([Ketcham, 2005](#)) we must relate the observed zonation in the analyzed surface to a model three dimensional distribution in the entire crystal, and then develop an appropriate (simplified) geometric model that captures the effects of this zonation model on the properties of interest (specifically the α ejection correction and He diffusion behavior). As a practical matter we adopt a spherical geometry to allow us to use widely available computational tools, especially the HeFTy helium production–diffusion code ([Ketcham, 2005](#)). The validity of the spherical approximation has been demonstrated by numerous previous workers ([Meesters and Dunai, 2002](#); [Farley et al., 2010](#); [Gautheron and Tassan-Got, 2010](#); [Watson et al., 2010](#)).

The LA-ICPMS concentration maps characterize a single slice through the three-dimensional concentration distribution in the crystal. In principle one could build up a fairly detailed view of the concentration distribution with repeated cycles of polishing followed by laser ablation analysis, but in practice it is difficult to obtain more than two or three such slices. Thus in general it is necessary to assume that the observed slice is representative of the distribution in the entire grain. We adopt a two-stage approach. In the first stage we convert the measured eU distribution into

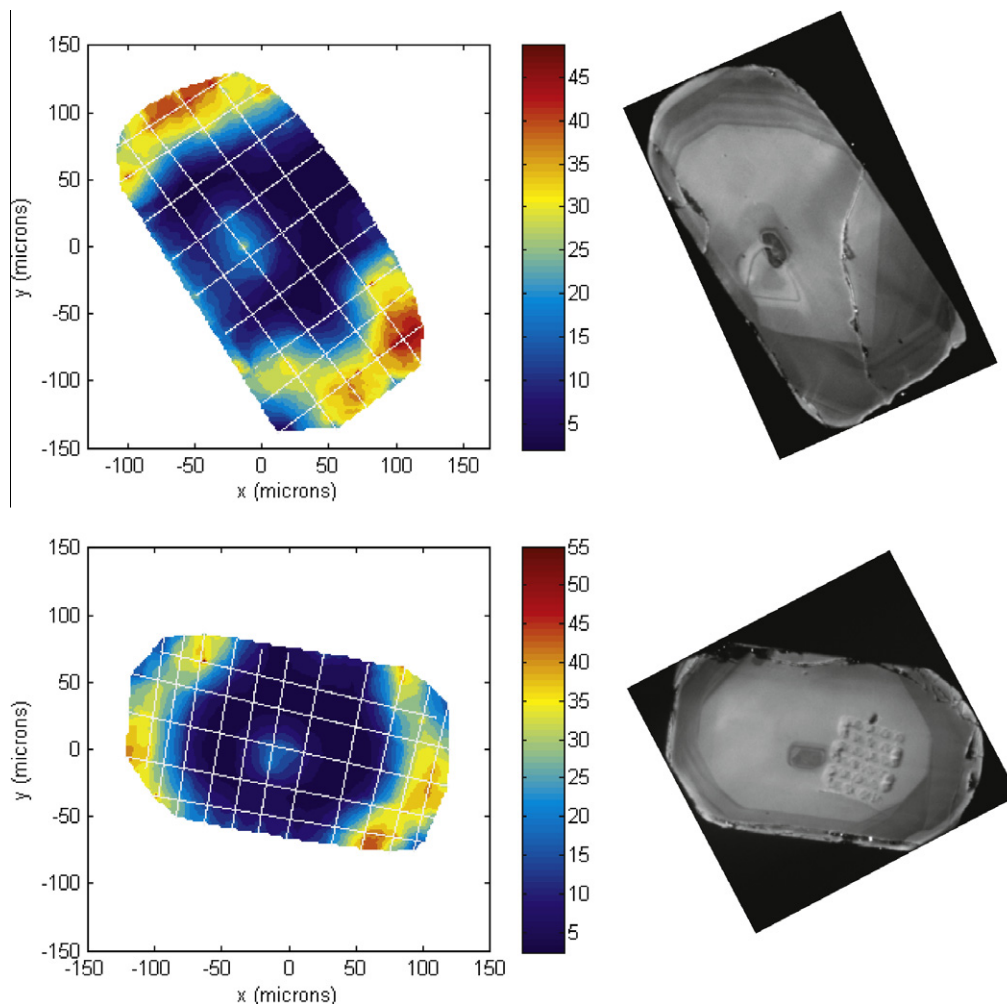


Fig. 3. Color-ramp map of U concentrations (in ppm) compared with chemical contrast detected by VPSE detector for two GC863 apatite grains. White lines indicate laser ablation trajectories. (A) Grain 4 (B) Grain 3; the rippled surface seen in part of the VPSE image is surface topography from a previous laser ablation measurement.

a cylinder with an eU distribution that is concentrically zoned about the cylinder axis. We then convert this cylinder into a sphere that has the same volume-weighted eU distribution. Specifically, we make the following assumptions:

- (1) the analyzed slice is in the mid-plane of the crystal, which is polished parallel to the c -axis.
- (2) the crystal can be approximated as a cylinder (Supplementary Fig. S2) of half-length Z and radius R_{cyl} .
- (3) following the geometric model of Watson et al. (2010), the grain is viewed as a series of concentric rings centered on the cylinder axis and stacked along the length of the cylinder (Supplementary Fig. S2; see also Fig. 4 of Watson et al. (2010)).
- (4) the concentration of each ring (C_{ring}) is equivalent to the mean of the two (generally different) concentrations observed where that ring intersects the analyzed surface (C_1 and C_2 in Supplementary Fig. S2). We are thus explicitly assuming that the properties of interest are adequately captured by the mean distribution (justification for this assumption is provided below).

The net result of these transformations is a model cylindrical crystal that is concentrically zoned and symmetric about the c -axis.

Existing He production–diffusion models assume a spherical diffusion geometry (although new geometric models have been developed (Gautheron and Tassan-Got, 2010) which may ultimately be incorporated into production–diffusion models). To convert the concentric cylinder into an “equivalent sphere”, we make the following transformations:

- (1) each ring represents a specific volume of the grain. $V_{\text{ring}} = 2\pi r \Delta r \Delta z$ where r is the distance from the cylinder axis to the center of the ring and Δr and Δz are the infinitesimal width and height of the ring (Supplementary Fig. S2).
- (2) each ring is located a specific distance D from the nearest edge:

$$D = \min\{R_{\text{cyl}} - r; |z - Z|\} \quad (1)$$

where $||$ denotes absolute value.

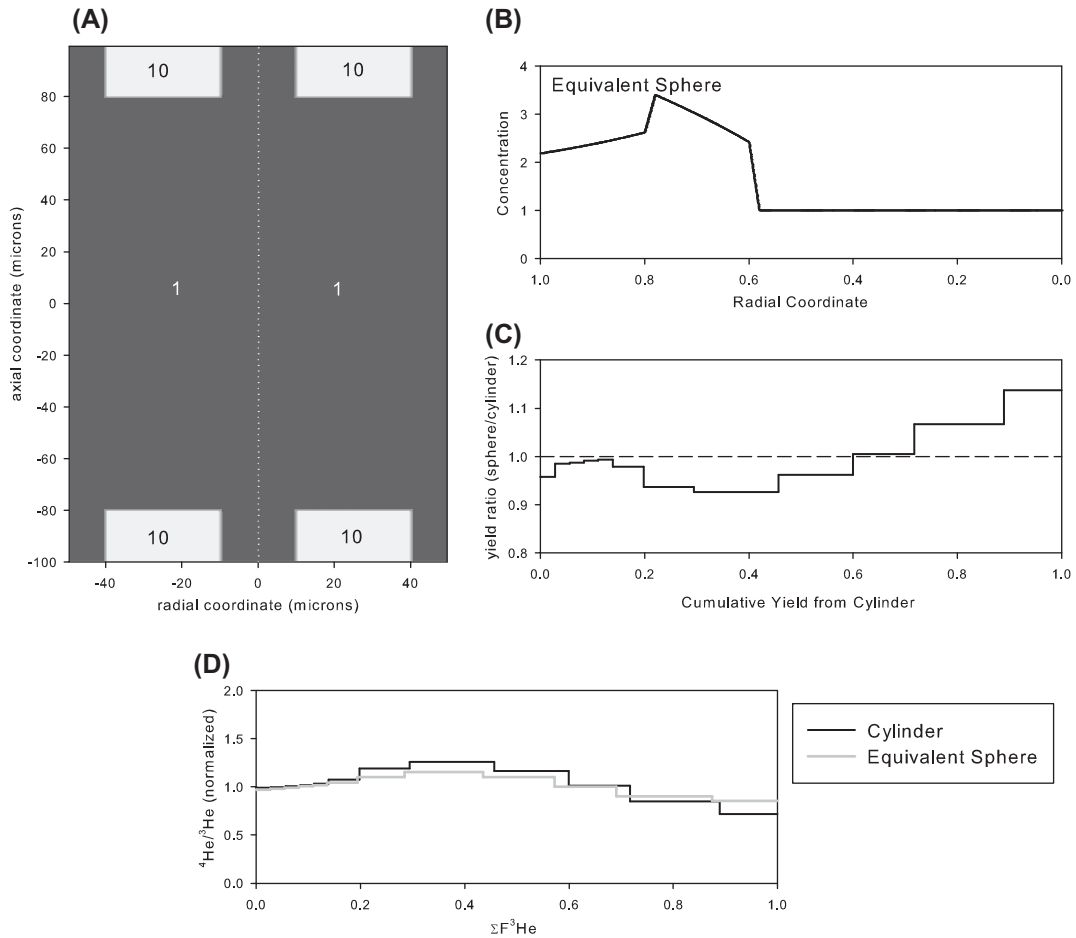


Fig. 4. Comparison of a zoned cylinder and its equivalent spherical representation in terms of diffusion yield and $^4\text{He}/^3\text{He}$ evolution. (A) Concentration distribution in cylinder; numbers indicate concentration in each region. (B) The equivalent spherical representation of the cylinder shown in part A (radial coordinate = 1 is grain rim). (C) Ratio of the yields obtained from the cylinder and its equivalent sphere during a simulated step heat. (D) Comparison of $^4\text{He}/^3\text{He}$ spectra obtained from the cylinder and its equivalent sphere. More examples are shown in Supplementary Fig. S3–S5.

Here z is the distance from the center of the ring to the cylinder midplane (defined to be $z = 0$). For the sake of simplicity we discretize the distances into N equally spaced bins.

Based on these calculations we can characterize the mean volume-weighted concentration in the cylinder at a given distance D from the cylinder edge, $C(D)$, as a function of D .

$$C(D)_{\text{cyl}} = \frac{\sum V_{\text{ring}}(D)C_{\text{ring}}(D)}{\sum V_{\text{ring}}(D)} \quad (2)$$

where the summation is over all rings with discrete distance D from the nearest edge.

- (3) we then assert that the “equivalent sphere” is simply the concentrically-zoned sphere that has the same concentration distribution relative to the grain edge as the cylinder, i.e., the same function $C(D)$.

We first establish the radius of the equivalent sphere. As shown previously, for both α ejection (Farley et al., 1996; Hourigan et al., 2005) and diffusion (Meesters and Dunai, 2002; Watson et al., 2010) approximate equivalence is

obtained when surface to volume ratios are equal. Thus the radius of the equivalent sphere is (Watson et al., 2010):

$$R_{\text{sph}} = 3R_{\text{cyl}}Z/(2Z + R_{\text{cyl}}) \quad (3)$$

The mean concentration at a distance D from the edge of the concentrically-zoned sphere is

$$D = R_{\text{sph}} - a \quad (4)$$

where a is the radial coordinate

$$C(D)_{\text{sph}} = C(R_{\text{sph}} - a) \quad (5)$$

We then equate the cylindrical and spherical distributions to get the concentration distribution in the sphere:

$$C(D)_{\text{sph}} = C(D)_{\text{cyl}} = C(R_{\text{sph}} - a) \quad (6)$$

One obvious benefit of this approach is that it ensures that the α ejection correction for the two representations will be very similar because the distribution of concentration near the grain edge (equated in the two representations) is what controls F_T (Farley et al., 1996; Hourigan et al., 2005).

To demonstrate the approach and to illustrate how well the equivalent sphere approach works for simulations of He diffusion behavior, in this section we compare results obtained from a model cylinder with results obtained on its equivalent sphere. Note that this is purely a comparison of the mathematical transformation and does not include the effects of either α redistribution nor of the averaging caused by the laser ablation analysis mentioned above. By making this comparison using multiple different patterns we conclude that the transformation is reasonably accurate for arbitrary patterns, including those produced by α redistribution and laser ablation averaging.

We present examples for four different arbitrarily selected styles of zonation shown in Fig. 4 and S4–S6. The first two models assume a patchy eU concentration distribution, while the second two assume concentric zonation. The assumed intracrystalline eU concentration variability ranges from a factor of 5 to a factor of 10 in the four models. In all models the assumed concentration distribution is identical in the four quadrants of the analyzed slice (i.e., the concentrations in one quadrant are mirrored across both the cylinder midplane and the c -axis to obtain the other three quadrants). This symmetry is required to permit the use of a modified version of CYLMOD (Watson et al., 2010) to evaluate the match in He diffusion behavior between the starting cylindrical model and its equivalent sphere representation. The models assume a cylinder with $R_{\text{cyl}} = 50 \mu\text{m}$ and $Z = 100 \mu\text{m}$, which has an equivalent sphere radius $R_{\text{sph}} = 60 \mu\text{m}$. Fig. 4 and S4–S6 show both the original map-view eU concentration and the equivalent sphere eU distribution computed as described above.

We test the similarity in diffusion release behavior of the original cylinder distribution with that from the equivalent sphere in two ways. First, we compute the ^4He fractional yields that would be obtained from each of the two representations in a simulated 12-step heating schedule assuming Durango apatite He diffusion kinetics (Farley, 2000). We assume isotropic diffusion and for the cylinder we compute the yields using a version of CYLMOD (Watson et al., 2010) that permits spatially varying concentrations. For the sphere we use a Fourier transform solution from Carslaw and Jaeger (1986). To assess the similarity of the ^4He yield response of the two representations we plot the ratio of the sphere yield to the cylinder yield as a function of the cumulative cylinder yield (Fig. 4C). Here perfect agreement between the two representations would plot as a horizontal line at unity.

As a second test, we also compute simulated $^4\text{He}/^3\text{He}$ spectra for the two representations using the same step heat schedule. In this case the ^4He yields obtained above are divided by simulated yields using the same heating schedule but assuming a homogeneous concentration distribution (reflecting a uniform distribution of ^3He) and the same geometric model. In this case perfect agreement between the two representations would be indicated by spectra that plot one atop the other.

As shown in Fig. 4 and S4–S6, the computed ^4He diffusion yield ratios display a small amount of structure, but are always within 13% of unity (usually much closer). Given the 5–10-fold variation in concentration across the model

grains, this agreement indicates that the equivalent sphere with its concentric zonation is surprisingly successful at capturing the initial distribution in the cylinder in terms of its impact on diffusive loss. To put the yield discrepancy in context, aliquots of Durango apatite held at 250 and 246 °C for 30 min would also have a 13% relative difference in yield based on published diffusion parameters (Farley, 2000). Together these observations suggest that forward models that compute He ages on specified time–temperature paths using the equivalent sphere representation will yield He ages which are in general in good agreement with those that would be obtained from the cylindrical representation and its heterogeneous ^4He distribution.

Similarly, as shown in Fig. 4 and S4–S6, in all four models the two representations yield remarkably similar $^4\text{He}/^3\text{He}$ spectra. Although perhaps surprising, the $^4\text{He}/^3\text{He}$ spectra produced from sharp and extremely patchy zonation in a cylinder (e.g., Fig. 4A) are almost identical to those produced by radially symmetric and more gradual concentration variations in the equivalent sphere.

We conclude that the equivalent sphere approach can be used to model both He ages and $^4\text{He}/^3\text{He}$ spectra for samples in which just a single section of the grain has been characterized for its eU distribution. While the agreement between the two representations is not perfect, it seems likely that the basic assumption required of the method – that the single analyzed slice is representative of the entire crystal – introduces a substantially larger source of error than the cylinder–sphere transformation.

4. RESULTS FROM SAMPLE GC863

4.1. Concentration maps, spherical equivalents, and inter-element correlations

Maps of U, Th and Ce were obtained on 19 separate apatite crystals from sample GC863. Eleven of these grains were analyzed, polished down to eliminate laser ablation damage, and re-analyzed; these grains have a “–2” or “RD2” designation after the sample name. Prior to the LA-ICPMS analysis several of the grains were analyzed on an SEM using a VPSE detector to characterize chemical contrast for comparison with the U, Th and Ce results. No attempt was made to determine the elements responsible for the contrast observed by the VPSE detector. Also prior to the LA-ICPMS analysis, several of the crystals were out-gassed in a $^4\text{He}/^3\text{He}$ experiment (Shuster and Farley, 2004).

Our measurements clearly reveal that sample GC863 is zoned in all three trace elements and in VPSE contrast. As shown for two crystals in Fig. 3, dark regions in VPSE contrast occur in a concentric ring that is thickest near the grain terminations. Dark regions also occur as isolated islands within bright cores. The concentric pattern is seen in nearly every apatite grain in the GC863 mount; the islands are only occasionally present. Fig. 3 reveals that the dark regions in VPSE contrast correspond to areas of higher U concentration (40 ppm) compared to brighter regions (~12 ppm). The darker regions also correspond to higher Th and Ce concentrations (Supplementary Fig. S7). These correlations lend support to the general validity of the laser

ablation results as well as to the suggestion (Jolivet et al., 2003) that SEM studies can provide at least qualitative evidence for U and Th zonation.

Concentration maps of the three trace elements and of eU for all 30 analyses are presented in Figure S7. The eU patterns shown in Fig. 3 are typical of the population – almost all grains have higher U, Th, and Ce concentrations on their rims, and these rims vary in thickness within and between grains. Maximum intra-crystal contrasts in U, Th, and eU are typically a factor of 2–3. Some analyses (e.g., “D8-2”, “F”) in addition have an island (or peninsula) of higher concentration in the interior, just like those in Fig. 3. While in some cases the pair of maps obtained at different depths by repolishing of a single crystal yield very similar concentration patterns (e.g., “O” and “O-2”), in other cases the patterns are quite different (e.g., “D5”, “D5-2”) Most of the differences can be rationalized as slices taken at different depths through a grain with a variable thickness high-concentration rim, especially if the slices are not perfectly parallel to the *c*-axis (i.e., grain is tilted on the mount). These observations underscore the fact that a single slice does not completely characterize the distribution of trace elements in the grain.

As shown for five representative GC863 grains, elemental cross plots (Fig. 5) reveal a strong correlation between U and Th both within each grain and among all the analyzed grains (mean Th/U = 0.44). In contrast the intra-grain correlations between Ce and U, Ce and Th, and Ce and eU are much weaker. For example, Fig. 5B shows only a broad correlation between Ce and eU within each of these five crystals, and in aggregate the eU/Ce ratio varies over a factor of ~7, from 0.013 to 0.085. This variability would make it difficult to quantitatively predict eU zonation from electron microprobe measurements of Ce. As with SEM images, the Ce contents are suggestive of eU zonation, but do not provide a quantitative proxy.

Using the computational approach described in Section 4 we converted the 30 eU maps (Supplementary Fig. S7) into their spherical equivalent eU concentration profiles (Fig. 6). The profiles are divided into two types of patterns: those that show a remarkably similar core to rim eU increase of about a factor of 3 (14 analyses) and those that do not (16 analyses). By comparison with the eU maps it is clear that the common pattern arises from the enriched rims (and especially the terminations) found on most grains. Among those that do not show this core-to rim increase,

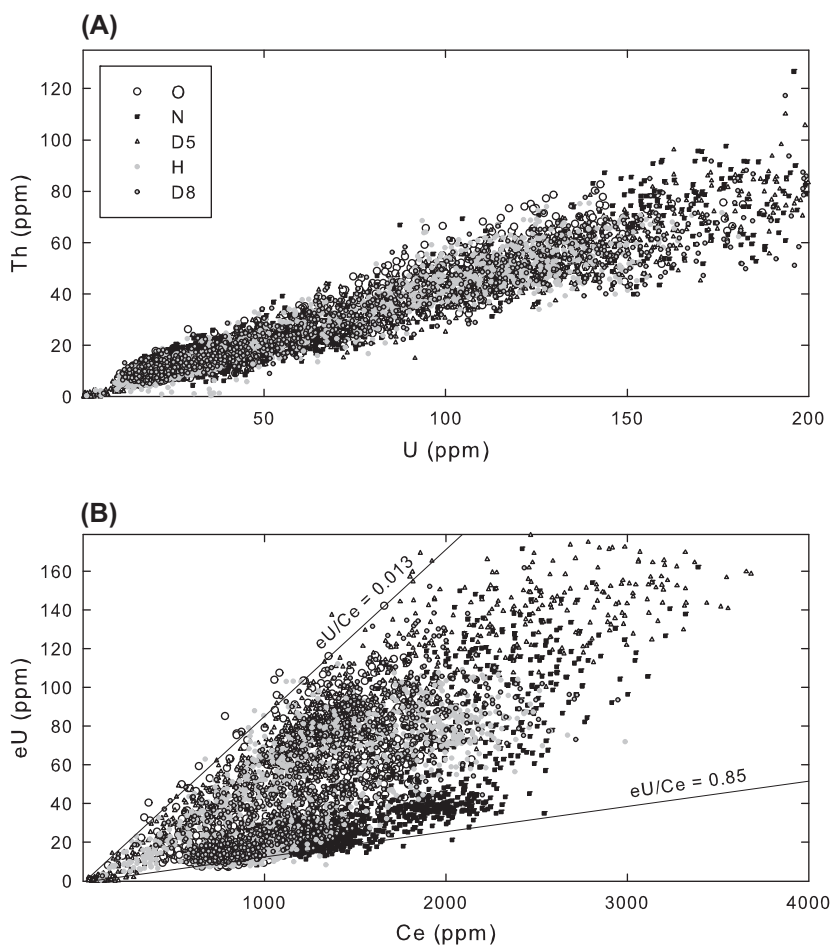


Fig. 5. Elemental cross plots for five representative GC863 apatite grains. (A) there is a very strong correlation of Th with U (mean Th/U = 0.44; $r^2 = 0.95$) both within a grain and among all analyzed grains in this sample; (B) the eU–Ce correlation is much weaker within individual grains, and the eU/Ce ratio varies widely among the grains (bounding slopes indicated).

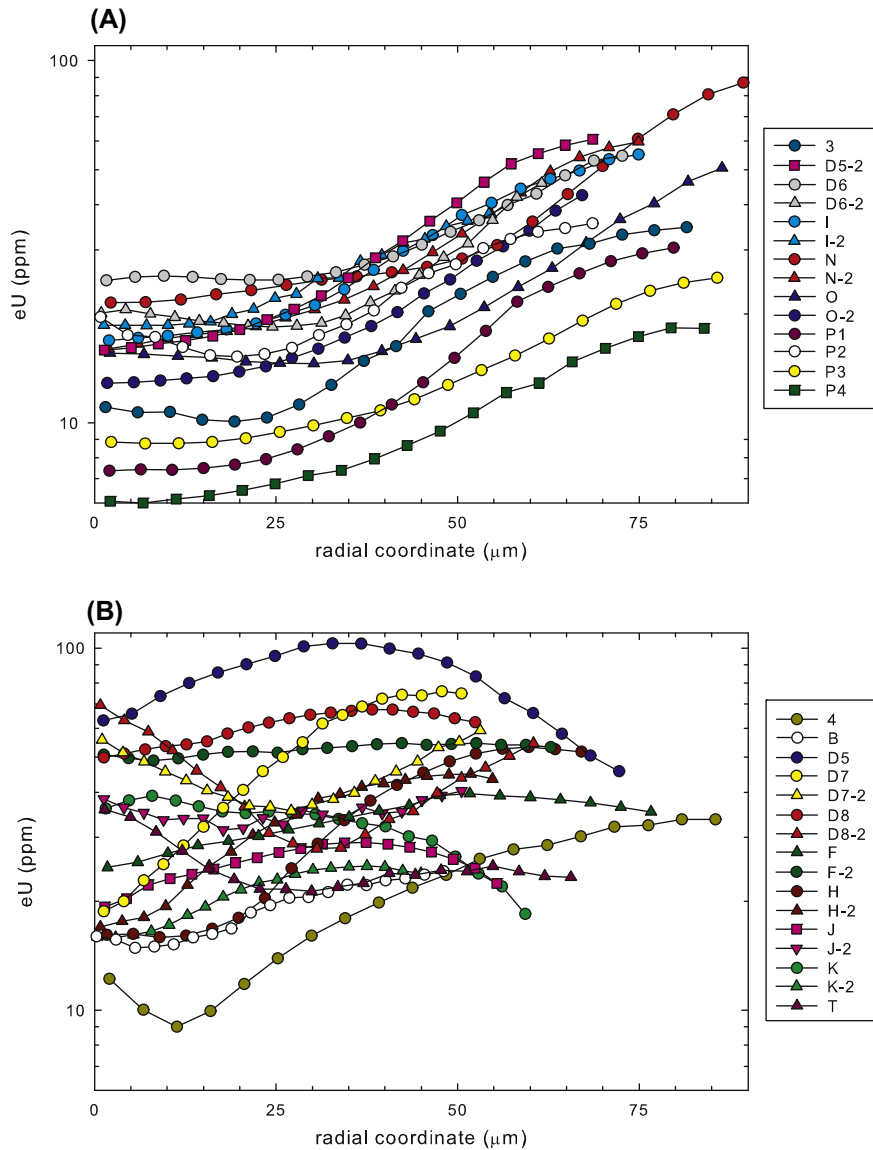


Fig. 6. Spherical equivalent eU zonation patterns for the 30 analyses of apatites from GC863. (A) analyses that conform to the “common pattern” of a smooth ~ 3 -fold increase from core to rim; (B) analyses that are distinct from the common pattern.

there is a fairly broad range of patterns. Several (e.g., “4”, “D8-2”) have high concentrations in the core and on the rim, with an intermediate region of low concentration. These are the analyses with an island or peninsula of high concentration in the grain core. A few rare grains have a nearly uniform spherical equivalent eU profile, but this arises from spatial averaging rather than homogeneity. For example, the uniform profile of Grain “F-2” occurs because a zone of high concentration extends almost exactly half-way across the grain such that it is coincidentally averaged out in the spherical equivalent computation.

4.2. Consequences for the α ejection correction

To assess the consequences of this degree of parent nuclide zonation for (U–Th)/He thermochronometry, we first computed for each analysis the α ejection factor assuming a

homogeneous distribution (here denoted F_{TH}) and then for the zoned case (F_{TZ}) based on the profiles shown in Fig. 6 using published equations (Farley et al., 1996). As noted in Section 2, we explicitly equate the eU patterns with the α particle distribution. The consequences of erroneous α ejection correction (i.e., use of F_{TH} rather than F_{TZ}) on (U–Th)/He ages is independent of any effects arising from diffusion down an inhomogeneous concentration gradient, so we consider the two effects separately. Because there are variations in grain dimension among the analyzed samples which induce variations in F_{TH} , we focus on the ratio F_{TZ}/F_{TH} . This ratio is a direct estimate of the error introduced by an erroneous (homogeneous) ejection correction. If this ratio is >1 , an inappropriately assumed F_{TH} would overcorrect for ejection and yield an age that is “too old”, while a ratio <1 does the opposite. As shown in Table 1, this ratio varies from 1.06 to 0.91 among the GC863 analyses. Within

Table 1

For each measured zonation pattern the table indicates the mean eU concentration, equivalent sphere radius, homogeneous and zoned α ejection factors (F_{TH} and F_{TZ} , respectively), and difference in closure temperature between the zoned and homogenous cases computed from RDAAM or Durango diffusion kinetics for the indicated cooling rates.

Sample	Mean eU (ppm)	Sphere R (μm)	F_{TZ}	F_{TH}	F_{TZ}/F_{TH}	Delta Tc (zoned-homogeneous)			
						RDAAM		Durango	
						10 C/Myr	1 C/Myr	10 C/Myr	1 C/Myr
Common pattern									
3	27	82	0.79	0.83	0.96	-2.1	-0.1	-2.1	-1.8
D5-2	44	75	0.76	0.81	0.94	-2.7	-0.3	-2.7	-2.4
D6	40	64	0.73	0.78	0.94	-2.2	-0.8	-2.4	-2.1
D6-2	30	69	0.74	0.79	0.93	-2.8	-0.7	-2.9	-2.7
I	41	83	0.79	0.83	0.95	-2.2	0.0	-2.3	-2.1
I-2	30	63	0.74	0.77	0.96	-1.3	-0.5	-1.6	-1.0
N	53	78	0.75	0.82	0.91	-3.6	0.1	-3.8	-3.5
N-2	42	85	0.78	0.83	0.94	-2.9	-0.1	-2.9	-2.6
O	32	96	0.80	0.85	0.93	-3.5	0.0	-3.4	-3.1
O-2	30	78	0.75	0.82	0.92	-3.4	-0.5	-3.4	-3.0
P1	22	80	0.77	0.82	0.94	-3.1	-0.2	-2.9	-2.7
P2	28	69	0.75	0.79	0.95	-1.9	-0.4	-1.9	-1.7
P3	19	86	0.79	0.83	0.95	-2.6	-0.4	-2.5	-2.2
P4			0.79	0.83	0.95	-2.5	-0.7	-2.5	-2.2
				Mean	0.94				
Other									
4	29	86	0.81	0.83	0.97	-1.5	-0.3	-1.5	-1.3
B	22	48	0.69	0.70	0.98	-0.9	-0.3	-0.8	-0.8
D5	74	78	0.86	0.82	1.06	2.2	1.7	2.2	2.0
D7	66	52	0.70	0.73	0.96	-1.2	-0.2	-1.5	-1.3
D7-2	46	63	0.74	0.77	0.96	-1.4	-0.6	-1.5	-1.3
D8	65	61	0.77	0.77	1.00	-0.1	-0.2	0.1	0.0
D8-2	41	70	0.76	0.80	0.96	-1.7	-0.7	-1.8	-1.6
F	37	91	0.85	0.84	1.00	0.0	0.1	0.0	-0.1
F-2	54	77	0.82	0.82	1.00	-0.1	-0.1	-0.1	-0.1
H	46	74	0.78	0.81	0.97	-1.5	0.0	-1.5	-1.2
H-2	41	62	0.75	0.77	0.98	-0.8	-0.2	-0.8	-0.7
J	27	65	0.79	0.78	1.01	0.5	0.0	0.5	0.6
J-2	36	60	0.75	0.76	0.99	-0.5	-0.3	-0.7	-0.5
K	28	71	0.83	0.80	1.04	1.7	1.4	1.6	1.5
K-2	24	56	0.74	0.75	0.99	-0.4	-0.2	-0.4	-0.3
T	24	66	0.78	0.78	1.00	-0.1	-0.1	-0.1	-0.1
				Mean	0.99				
				Grand mean	0.97				

the grains with the common pattern, the ratio is low and fairly uniform: 0.91–0.96. The ratio is higher and more variable in the other patterns: 0.96–1.06.

If we imagine that each of the patterns in Fig. 6 is an independent realization of the eU zonation within one crystal in this population, we can use these results to estimate both the inaccuracy in the ejection-corrected (U–Th)/He age (i.e., deviation from the true age obtained if the ejection correction were made accurately) and the age scatter. The ejection-corrected age can be approximated to sufficient accuracy as He age = raw age/ F_T . Based on the values in Table 1 we calculate that erroneous use of the homogenous correction factor F_{TH} from this population of apatites would yield a mean He age that is 3.3% too young with a total range among aliquots of +6% to –9%. This range far exceeds the typical analytical uncertainty of a few % on He age determinations, but is typical of the reproducibility observed in apatite He dating studies. As pointed out

previously (Farley et al., 1996), neither abrasion nor reporting of ages uncorrected for ejection can eliminate the age error arising from the use of F_{TH} for a grain that is zoned, although its magnitude would be different if either of these approaches were adopted. This is because in a zoned crystal there is in general nowhere that injection and ejection are balanced (as would be required for these approaches to yield accurate ages).

4.3. Zoning effects on diffusive He loss

The second issue to consider is how the heterogeneous concentration profile affects diffusive He loss. In this case the consequences of assuming homogeneity when in reality an apatite is zoned depend on the cooling history. For example, aside from the α ejection effect described above, an apatite that is cooled instantly would be unaffected by this phenomenon, while one that resides for a long period

in the He partial retention zone, where diffusion is important, may be significantly affected.

Recent additions to the HeFTy computer program (Ketcham, 2005) allow various aspects of this problem to be studied relatively easily. The implementation of the RDAAM diffusivity calibration (Flowers et al., 2009) has been combined with previous functionality allowing radial zoning in U and Th, and incorporates the evolution of radially varying diffusivity due to local radiation damage. When RDAAM is the selected diffusion model, the diffusivity at each radial coordinate is a function of the radiation damage caused by U, Th and Sm concentration at that location, and subsequent annealing, even if the “redistribution” method for accounting for long α stopping distances is used. It thus conceptually corresponds to α recoil causing the diffusion-altering damage, as opposed to fission tracks or α particles which would spread damage over a multi-micron region. Another addition to HeFTy is the calculation of $^4\text{He}/^3\text{He}$ spectra according to principles laid out by Shuster and Farley (2005). The $^4\text{He}/^3\text{He}$ spectra calculations account for zoning in U and Th, but do not include radiation damage alteration of diffusivity during the simulated step-heat used to generate the spectrum. We believe that the latter detail is unnecessary because ^4He and ^3He will be equally affected by diffusivity variation, and thus their ratio will be unchanged.

We used HeFTy to compute He ages from the zoned concentration profiles in Fig. 6 on two different cooling paths. We assumed constant cooling rates of either 10 or 1 °C/Ma, which allow us to convert the ages into effective closure temperatures (by adding the product of the predicted age and the cooling rate to the final model temperature). We assumed either Durango (Farley, 2000) or

RDAAM (Flowers et al., 2009) He diffusion kinetics. We used the “ejection only” option to prevent HeFTy from redistributing α particles within the grain (i.e., so that the input eU profile is used for the He distribution). For the reference case for each grain we assumed a homogenous concentration equivalent to the mean concentration computed from the LA-ICPMS results, and used the homogenous ejection correction factor (F_{TH}) appropriate for the grain’s radius. This was then compared to results obtained from the eU distributions shown in Fig. 6, ejection corrected using the zoned correction factor F_{TZ} . Because in the latter simulations the ejection correction is accurately handled, the only difference between the zoned and unzoned scenarios is the distribution of diffusant. As shown in Table 1, apparent closure temperatures are lower in grains with enriched rims and higher in grains with depleted rims relative to the homogeneous case. The effect is relatively small in the GC863 analyses, ranging from about +2 to –4 C. To illustrate this effect Fig. 7 plots the difference in apparent closure temperature between the zoned and unzoned scenarios as a function of the ratio $F_{\text{TZ}}/F_{\text{TH}}$. This ratio is simply a convenient way to characterize the zonation pattern; values <1 indicate rim enrichment, while values >1 indicate rim depletion. For both of the Durango cases and for the RDAAM case at 10 °C/Ma cooling rate there is a strong positive correlation between these two variables, largely independent of cooling rate and kinetic model. This correlation arises from the fact that when more He is present near the grain edge, relatively more is lost by diffusion at any given temperature. Thus the two factors – erroneous α ejection correction and the consequences of zonation on diffusion – act in the same direction to bias the He age away

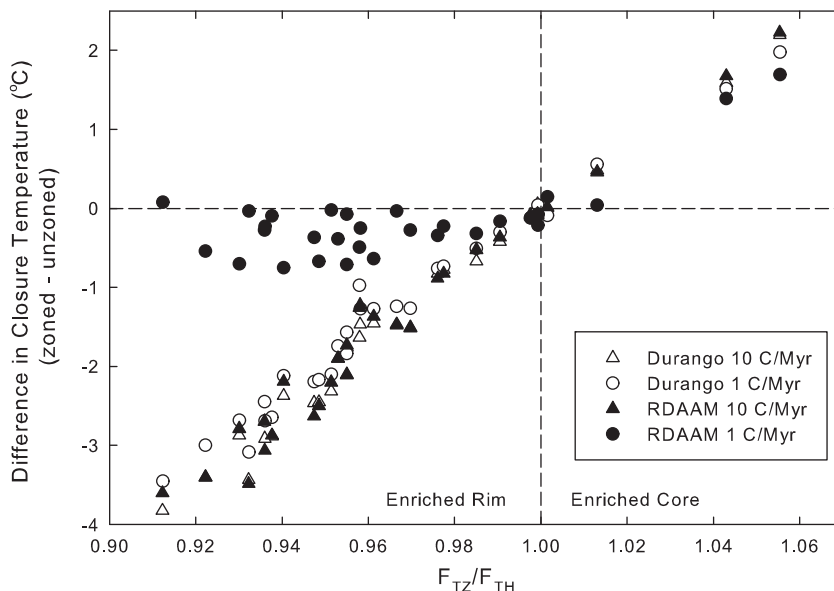


Fig. 7. The effects of eU zonation on He closure temperature arising solely from the shape of the concentration profile. The ratio $F_{\text{TZ}}/F_{\text{TH}}$ is a convenient measure of the magnitude and style of eU zonation. Each point represents a computation for one of the 30 eU profiles shown in Fig. 6 using one of the four indicated combinations of kinetic model and cooling rate. While in general there is a strong correlation between these two parameters, such that grains with eU-enriched rims have lower closure temperatures, this pattern breaks down at slow cooling rates when using RDAAM. This discrepancy is a result of the generation of enhanced retentivity in the eU-enriched regions during protracted cooling.

from that expected for eU homogeneity. For example, consider analysis “D6-2”, which is typical of the common pattern in GC863. When cooled at 1 °C/Ma and using Durango kinetics, HeFTy predicts that a crystal of the size of “D6-2” with a homogeneous He distribution would yield an ejection corrected He age of ~56 Ma. However, when the eU pattern in analysis “D6-2” is subjected to the same cooling path, the predicted ejection-corrected age is ~50 Ma. Of this 6 Ma discrepancy, ~2.5 Ma arises from the effects of diffusion, and 3.5 Ma from the α ejection correction.

In the case of RDAAM kinetics and a cooling rate of 1 °C/Ma the results are quite different (Fig. 7). Rather than declining steadily with F_{TZ}/F_{TH} , in the slowly-cooled RDAAM case the difference in apparent closure temperatures levels off near zero. This distinction must arise from the fact that intracrystalline variations in eU and thus radiation damage are acting to impede He diffusion preferentially in the outer portion of the grain. The effect is manifest at slow cooling rates because slow cooling permits the accumulation of enough radiation damage to produce an effect. Why the competing effects of rim-enrichment in diffusant and preferential accumulation of radiation damage on the rim should come so close to compensating in terms of closure temperature is unclear. Further work is needed to understand this effect and to assess whether (and under what circumstances) the radiation effect may dominate, such that apparent closure temperatures actually rise with the extent of rim enrichment.

Earlier modeling work showed that a factor of three eU zonation, similar to that observed in GC863, yields readily observable effects on $^4\text{He}/^3\text{He}$ spectra (Farley et al., 2010). To further demonstrate this result we modeled $^4\text{He}/^3\text{He}$ spectra for our samples using HeFTy. In particular we computed normalized age spectra. A normalized age spectrum is the $^4\text{He}/^3\text{He}$ ratio obtained in each step divided by the $^4\text{He}/^3\text{He}$ ratio that would be obtained in that step from a homogeneous distribution of ^4He subject to α ejection (Shuster and Farley, 2005); this is in effect what would be reported (or modeled) in the absence of information on zonation (Shuster and Farley, 2004). A normalized age spectrum has the advantage that, were eU homogeneous, the effects of α ejection are eliminated from the plot, allowing more direct focus on other important factors such as diffusion or inhomogeneity of the production function.

As discussed previously (Farley et al., 2010), the effects of zonation on $^4\text{He}/^3\text{He}$ spectra are most readily observed when there is no diffusion superimposed on the production function. Thus for this demonstration we modeled the extreme case of $^4\text{He}/^3\text{He}$ age spectra for the zonation patterns shown in Fig. 6 but with no diffusive loss (Fig. 8). As expected the model $^4\text{He}/^3\text{He}$ age spectra for the “common pattern” in GC863 are all broadly similar: an excess in $^4\text{He}/^3\text{He}$ of a few tens of percent in the earliest ^3He release. By mass balance these excesses become deficits towards the end of the ^3He release. The aliquot with the greatest $^4\text{He}/^3\text{He}$ excess (“N”) has the greatest core-to-rim eU contrast (about 4 \times), while the aliquot with the flattest model $^4\text{He}/^3\text{He}$ age spectrum (“I-2”) has a range of just under a factor of 2 in eU. Among the aliquots with the more diverse

patterns, several yield model $^4\text{He}/^3\text{He}$ age spectra very similar to those in the common pattern (e.g., “D7”, “D8-2”, “4”). The concentration profile for these aliquots define a *u*-shape, with a factor of 2–3 increase in concentration towards the grain rim from a minimum located between 10 and 35 μm from the grain center. Three patterns yielded $^4\text{He}/^3\text{He}$ age spectra with initial $^4\text{He}/^3\text{He}$ deficits (“J”, “K”, “D5”); while aliquot “K” has a steady core-to-rim concentration decrease, the other two aliquots have a mid-radius maximum in eU.

The important point arising from these patterns is that almost all of them are substantially different from the pattern expected for a uniform eU distribution (i.e., a horizontal line at unity in Fig. 8). Failure to recognize this heterogeneity would lead to either a spectrum that is impossible to interpret (e.g., because it plots in a region that is forbidden in a production–diffusion model (Shuster and Farley, 2004)) or to erroneous interpretation of the $^4\text{He}/^3\text{He}$ spectrum in terms of cooling history. This issue has been considered more fully from a theoretical perspective elsewhere (Farley et al., 2010).

4.4. Comparison with (U–Th)/He ages and $^4\text{He}/^3\text{He}$ spectra measured on sample GC863

Prior to laser ablation eU measurement, four of the GC863 grains (“D6”, “D8”, “F” and “O”) were analyzed for $^4\text{He}/^3\text{He}$ spectrum. This dataset allows us to investigate whether the expected consequences of eU zonation are actually observed in measured spectra. Fig. 9 shows that several of these spectra are unambiguously aberrant: the normalized age spectra have a maximum or hump early in the cumulative ^3He release. This pattern is inconsistent with a ^4He diffusion profile produced by a uniform distribution of U and Th, and instead suggests enrichment of eU near the crystal rims. These patterns cannot be directly compared to those in Fig. 8 because sample GC863 has experienced diffusive loss over geologic time. However we can use a published time–temperature path for samples from the same area to forward model the age spectra expected from these zoned grains. We use a time–temperature history proposed for the bottom of lower Granite Gorge (Wernicke, 2011). For each of these four grains a first eU map was obtained, the grain repolished, and a second eU map obtained. Thus we have two different eU profiles and thus predicted $^4\text{He}/^3\text{He}$ spectra for each grain. We also plot the $^4\text{He}/^3\text{He}$ spectrum predicted for a uniform eU distribution.

As shown in Fig. 9, the $^4\text{He}/^3\text{He}$ spectra predicted from the measured eU distributions do a far better job of capturing the observed behavior than does the uniform eU distribution. For example, the “hump” at $\Sigma F^3\text{He} \sim 0.1$ that is especially prevalent in aliquots “D6” and “O” is close to that predicted based on the intense rim-enrichment of eU in these two aliquots. The absence of this “hump” in Grain “F” is as predicted based on the near uniform eU obtained on this crystal.

While it is clear that the shape of the spectra are not perfectly reproduced, the gross similarity and internal consistency for all four grains is striking. The differences

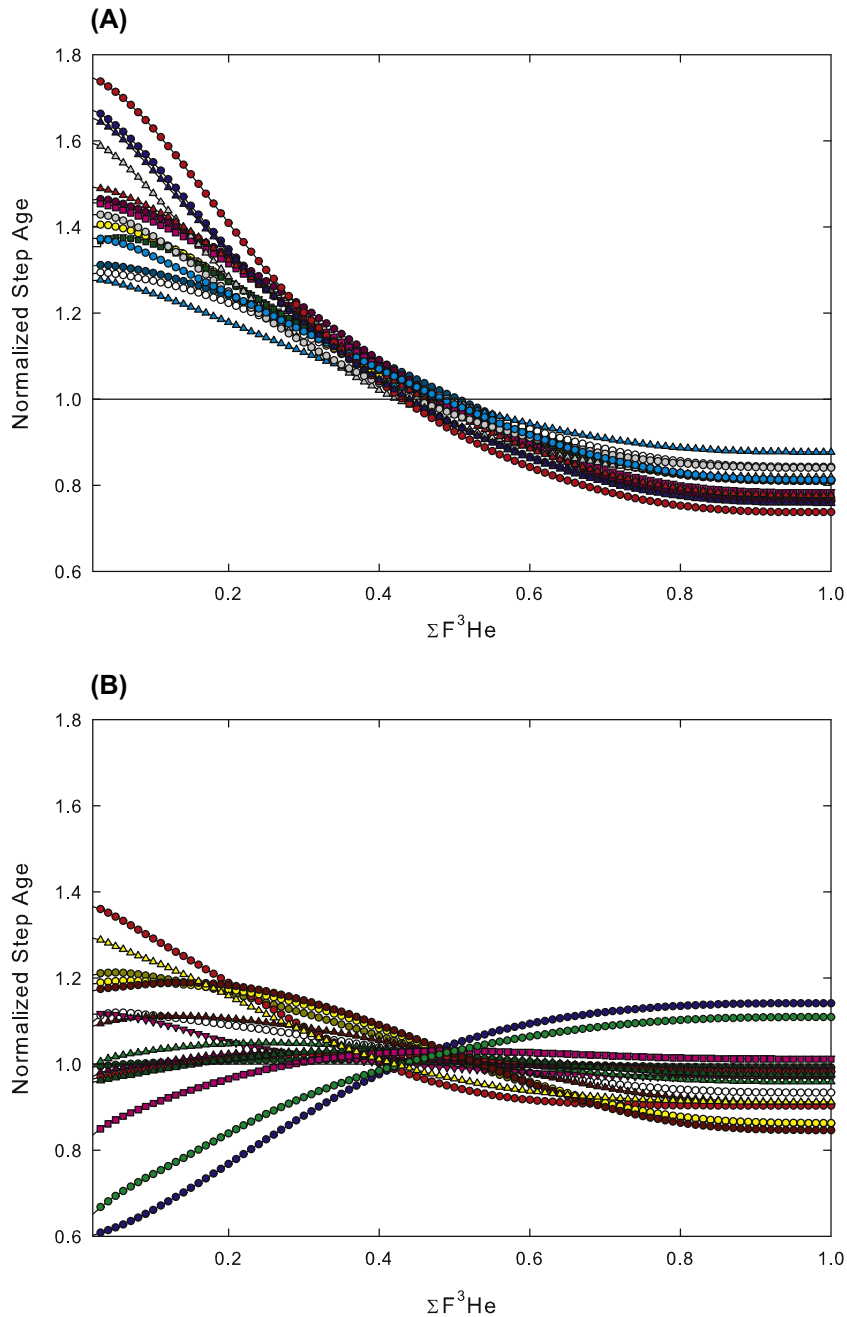


Fig. 8. Model $^4\text{He}/^3\text{He}$ age spectra for the 30 concentration profiles in Fig. 6. Symbols and colors match those in Fig. 6. (Panel A) includes all profiles exhibiting the common pattern in Fig. 6, while (B) shows all of the other profiles. Any points lying above a normalized step age of unity are inconsistent with diffusion from a uniform distribution of diffusant. (For interpretation of the references to colour in this figure legend, the reader is referred to the web version of this article.)

between predicted and observed spectra likely arise from errors in the assumed time–temperature path coupled with our limited information on the complete distribution of eU within the apatites and/or in our model to convert the measured slice into an equivalent spherical representation. In all but aliquot “D8” the two different estimates of the eU zonation pattern yield very similar model spectra, suggesting that even a single eU slice can assist the interpretation of $^4\text{He}/^3\text{He}$ spectra. These observations suggest that

combining $^4\text{He}/^3\text{He}$ spectra with eU mapping may provide a more robust means to obtain cooling histories on zoned apatites.

A similar comparison can be made with respect to the (U–Th)/He ages of GC863, though the ages were measured on a different population of grains than were mapped for eU. As noted previously, the standard deviation of the five individual GC863 (U–Th)/He ages is 3% (excluding one much older grain). Running all 30 of the eU profiles

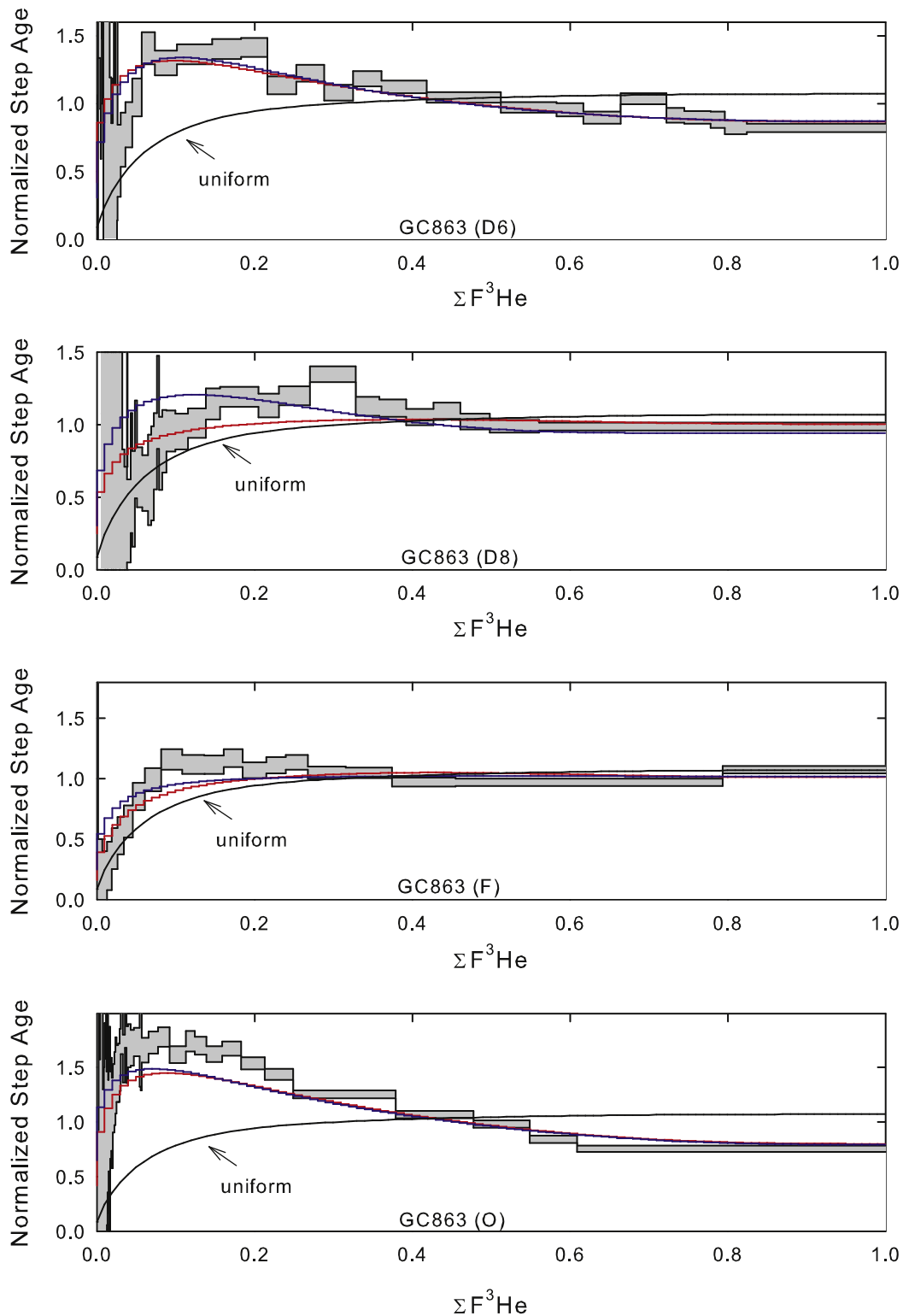


Fig. 9. Measured $^4\text{He}/^3\text{He}$ age spectra (normalized) compared with model results for GC863 crystals “D6”, “D8”, “F”, and “O”. The measured spectra are shown as grey boxes. The smooth black curve is the model spectrum for a uniform eU distribution and the time–temperature path assumed for Lower Granite Gorge. The red and blue curves were computed from the two eU patterns measured on each of these four crystals and again assuming the Lower Granite Gorge time–temperature path.

through HeFTy using the Lower Granite Gorge time–temperature path yields a standard deviation of about 6% on

the He ages. Thus the observed age scatter on five samples is smaller than predicted from the full range of 30 measured

eU patterns; this is as expected because the eU distribution is less completely sampled by the dated grains. The one He age outlier (about 30% higher than the five other grains) is far outside the range predicted from the eU profiles. Its anomalous age must arise either from a far more extreme degree of zonation than we measured, or more likely, from some other phenomenon.

5. CONCLUSIONS

Laser ablation ICPMS analyses of polished sections of apatite can readily document spatial variations in trace elements of interest for (U–Th)/He thermochronometry at the ppm level with a precision of about 5%. The spatial resolution of the resulting concentration distributions depends on the number of analytical traverses, the laser beam diameter, and the method used to interpolate the traverses into a regularized grid for mapping. The technique we developed here was chosen to produce a map with a spatial averaging of $\sim 20 \mu\text{m}$ radius across the entire section, comparable to the α particle stopping distance. This map can be converted into a concentration profile in an equivalent sphere, which allows the data to be incorporated into spherical He production–diffusion models with adequate accuracy. This conversion requires an assumption of how the analyzed section relates to the full-3D concentration pattern in the crystal. We assumed that the 3D pattern is radially symmetric about the c -axis. While the method was initially applied to apatite, it can be extended to zircon as well.

Using this method, 30 concentration maps produced on 19 different apatite crystals from a single granite from the Grand Canyon (GC863) were found to have significant concentration gradients in U, Th, Ce, and eU. Many of the analyzed grains have a systematic pattern of ~ 3 -fold enrichment of all three trace elements from core to rim. Correlations within and among grains are very strong for U and Th. In contrast there is only a moderate correlation between Ce and the actinides within individual grains, and the slope of the correlation varies between grains. Similarly, there is a notable visual correlation between the trace elements and the contrast detected by an SEM using a VPSE detector. Taken together these observations suggest that both SEM and electron microprobe analyses of Ce or other rare earth elements can be used to infer U,Th zonation (Jolivet et al., 2003), but probably not in a quantitative fashion.

To assess the consequences of this degree of zonation for apatite (U–Th)/He thermochronometry we assumed that each equivalent sphere pattern is applicable to a crystal in the apatite population in GC863. Modeling shows that these patterns have two consequences on (U–Th)/He ages. Regardless of cooling history, the α ejection correction factor for the zoned grains differs from the homogenous case. If computed using an ejection correction factor that assumes homogeneity, the ages obtained from these model grains would range from 91% to 106% of the value obtained if the correction were accurately made (mean $\sim 97\%$). Because α ejection corrections almost invariably assume homogeneity, this sample would yield both a slightly inaccurate (too young) corrected He age, as well as grain-to-grain scatter that far exceeds analytical uncertainty. An

additional effect arises from the concentration gradient and the accumulation of radiation damage, which each modify the rate of diffusive loss. These effects depend on cooling history, but for cooling rates of either 1 or $10^\circ\text{C}/\text{Ma}$ correspond to a shift in closure temperature of -4 to $+2$ C. The ejection correction and diffusion gradient effects are additive and tend to shift ages in the same direction. Our modeling suggests that for some cooling histories the damage accumulation effect may come to dominate, such that rim enrichment actually begins to raise the closure temperature. This possibility requires further investigation. Consistent with earlier modeling (Farley et al., 2010), the degree of zonation in GC863 also has important implications for $^4\text{He}/^3\text{He}$ profiles. A comparison between the modeled $^4\text{He}/^3\text{He}$ spectra of the zoned grains and the measured spectra suggests that the methodology developed here does a reasonably good job of characterizing the eU distribution and its consequences for He diffusion.

In the absence of a database of U, Th zonation in apatites, it is difficult to assess whether the zonation in GC863 is typical of apatites in general, and thus whether its predicted consequences are representative. However, since the effects of zonation may be readily apparent in both bulk ages and in $^4\text{He}/^3\text{He}$ spectra, further mapping of apatites seems worthwhile.

ACKNOWLEDGEMENTS

This work was supported by NSF Grants EAR-0738627 and EAR-0738474. D.L.S. acknowledges support from the Ann and Gordon Getty Foundation. We thank Mike Scott for his donation of the LA-ICPMS to Caltech and Yashna Peerthum for analytical assistance.

APPENDIX A. SUPPLEMENTARY DATA

Supplementary data associated with this article can be found, in the online version, at [doi:10.1016/j.gca.2011.05.020](https://doi.org/10.1016/j.gca.2011.05.020).

REFERENCES

- Belton D. X., Brown R. W., Kohn B. P., Fink D. and Farley K. A. (2004) Quantitative resolution of the debate over antiquity of the central Australian landscape: implications for the tectonic and geomorphic stability of cratonic interiors. *Earth and Planetary Science Letters* **219**, 21–34.
- Boyce J. W. and Hodges K. V. (2005) U and Th zoning in Cerro de Mercado (Durango, Mexico) fluorapatite: Insights regarding the impact of recoil redistribution of radiogenic He-4 on (U–Th)/He thermochronology. *Chemical Geology* **219**, 261–274.
- Carslaw H. S. and Jaeger J. C. (1986) *Conduction of Heat in Solids*, second ed. Oxford University Press, Oxford.
- Davidson J., Hassanzadeh J., Berzins R., Stockli D. F., Bashukoo B., Turrin B. and Pandamouz A. (2004) The geology of Damavand volcano, Alborz Mountains, northern Iran. *Geological Society of America Bulletin* **116**, 16–29.
- Ehlers T. A. and Farley K. A. (2003) Apatite (U–Th)/He thermochronometry: methods and applications to problems in tectonic and surface processes. *Earth and Planetary Science Letters* **206**, 1–14.

- Farley K. A. (2000) Helium diffusion from apatite: general behavior as illustrated by Durango fluorapatite. *Journal of Geophysical Research-Solid Earth* **105**, 2903–2914.
- Farley, K.A., 2002. (U–Th)/He dating: Techniques, calibrations, and Applications, Reviews In Mineralogy & Geochemistry, vol. 47, Washington, pp. 819–844.
- Farley K. A., Kohn B. P. and Pillans B. (2002) The effects of secular disequilibrium on (U–Th)/He systematics and dating of Quaternary volcanic zircon and apatite. *Earth and Planetary Science Letters* **201**, 117–125.
- Farley, K.A., Shuster, D.L., Watson, E.B., Wanser, K.H., Balco, G. 2010 Numerical investigations of apatite $^4\text{He}/^3\text{He}$ thermochronometry. *Geochemistry, Geophysics, Geosystems* doi:10.1029/2010GC003243.
- Farley K. A., Wolf R. A. and Silver L. T. (1996) The effects of long alpha-stopping distances on (U–Th)/He ages. *Geochimica et Cosmochimica Acta* **60**, 4223–4229.
- Flowers R. M., Ketcham R. A., Shuster D. L. and Farley K. A. (2009) Apatite (U–Th)/He thermochronometry using a radiation damage accumulation and annealing model. *Geochimica et Cosmochimica Acta* **73**, 2347–2365.
- Gautheron C. and Tassan-Got L. (2010) A Monte Carlo approach to diffusion applied to noble gas/helium thermochronology. *Chemical Geology* **273**, 212–224.
- Gautheron C., Tassan-Got L., Barbarand J. and Pagel M. (2009) Effect of alpha-damage annealing on apatite (U–Th)/He thermochronology. *Chemical Geology* **266**, 157–170.
- Green P. F., Crowhurst P. V., Duddy I. R., Japsen T. and Holford S. P. (2006) Conflicting (U–Th)/He and fission track ages in apatite: Enhanced He retention, not anomalous annealing behaviour. *Earth and Planetary Science Letters* **250**, 407–427.
- Hourigan J. K., Reiners P. W. and Brandon M. T. (2005) U–Th zonation-dependent alpha-ejection in (U–Th)/He chronometry. *Geochimica et Cosmochimica Acta* **69**, 3349–3365.
- Hurley P. M. (1954) The helium age method and the distribution and migration of helium in rocks. In *Nuclear Geology* (ed. H. Faul). John Wiley and Sons, New York, pp. 301–329.
- Jolivet M., Dempster T. and Cox R. (2003) Distribution of U and Th in apatites: implications for U–Th/He thermochronology. *Comptes Rendus Geoscience* **335**, 899–906.
- Ketcham R. A. (2005) Forward and inverse modeling of low-temperature thermochronometry data low-temperature thermochronology: techniques, interpretations, and applications, reviews. *Mineralogy & Geochemistry* **58**, 275–314.
- Lippolt H. J., Leitz M., Wernicke R. S. and Hagedorn B. (1994) (U+Th)/He dating of apatite: experience with samples from different geochemical environments. *Chemical Geology* **112**, 179–191.
- Meesters A. G. and Dunai T. J. (2002) Solving the production–diffusion equation for finite diffusion domains of various shapes Part 1. Implications for low-temperature (U–Th)/He thermochronology. *Chemical Geology* **186**, 333–344.
- Shepard, D. 1968 A two-dimensional interpolation function for irregularly-spaced data. *Proceedings of the 1968 ACM National Conference*. doi:10.1145/800186.810616, pp. 517–524.
- Shuster D. L. and Farley K. A. (2004) He-4/He-3 thermochronometry. *Earth and Planetary Science Letters* **217**, 1–17.
- Shuster D. L. and Farley K. A. (2005) He-4/He-3 thermochronometry: theory practice, and potential complications, low-temperature thermochronology: techniques, interpretations, and applications reviews. *Mineralogy & Geochemistry* **58**, 181–203.
- Shuster D. L. and Farley K. A. (2009) The influence of artificial radiation damage and thermal annealing on helium diffusion kinetics in apatite. *Geochimica et Cosmochimica Acta* **73**, 183–196.
- Strutt T. H. R. J. (1908) On the accumulation of helium in geological time. *Royal Society Proceedings* **80**, 272–277.
- Watson E. B., Wanser K. H. and Farley K. A. (2010) Anisotropic diffusion in a finite cylinder, with geochemical applications. *Geochimica et Cosmochimica Acta* **74**, 614–633.
- Wernicke, B.P. 2011 The California River and its role in carving Grand Canyon Geological Society of America Bulletin doi:10.1130/B30274.1.
- Wolf R. A., Farley K. A. and Kass D. M. (1998) A sensitivity analysis of the apatite (U–Th)/He thermochronometer. *Chemical Geology* **148**, 105–114.
- Zeitler P. K., Herczig A. L., McDougall I. and Honda M. (1987) U–Th–He dating of apatite: a potential thermochronometer. *Geochimica et Cosmochimica Acta* **51**, 2865–2868.

Associate editor: Peter Reiners